

# Assessment of intra-build variations in tensile strength in electron beam powder-bed fusion Ti-6Al-4V part 2: Effects of powder mixing

Nicholas Derimow<sup>1\*</sup>, Jake T. Benzing<sup>1</sup>, Orion L. Kafka<sup>1</sup>, Newell Moser<sup>1</sup>, Priya Pathare<sup>2</sup>, Michael Walker<sup>3</sup>, Frank W. DelRio<sup>2</sup>, Nikolas Hrabe<sup>1</sup>

<sup>1</sup>*Applied Chemicals and Materials Division, National Institute of Standards and Technology, 325 Broadway, Boulder, CO 80305, USA*

<sup>2</sup>*Sandia National Laboratories, Albuquerque, NM 87123 USA*

<sup>3</sup>*Colorado School of Mines, Golden, CO 80401 USA*

---

## Abstract

In Part 2 of this paper series, high-throughput tensile testing and characterization of porosity, microstructure, and oxygen content was carried out on Ti-6Al-4V samples that were fabricated via electron beam powder-bed fusion (PBF-EB) to test our hypothesis that current industrial powder mixing strategies lead to stochastic chemistry content and tensile property variation throughout a given build. Fifteen rectangular blocks were built at locations across the entire build plate and machined into high-throughput tensile racks that contained 25 mini tensile coupons each (375 total specimens). There was a spread of 138.9 MPa in yield strength (YS) across all specimens. Considering the YS spread was only 74.2 MPa for a virgin build with no mixing, as detailed in Part 1, the difference between these two YS ranges is expected to be attributed to mixing. To determine the cause for this observed spread in YS, systematic investigation of porosity, microstructure, and oxygen content was performed via scanning electron microscopy (SEM), micro X-ray computed tomography ( $\mu$ XCT), inert gas fusion, and time-of-flight secondary ion mass spectrometry (ToF-SIMS). The large variation in YS for these specimens could not be attributed to internal porosity, fracture surface porosity,  $\alpha$ -lath thickness, or crystallographic texture. Inert gas fusion measurements indicated large, stochastic variation in oxygen content, and measurements via ToF-SIMS near the fracture surfaces indicate localized chemistry variations that could be responsible for the large variations in tensile properties, specifically the yield strength. Specific alternative powder mixing and reuse methodologies are proposed to mitigate undesirable chemistry and tensile property variation within PBF-EB Ti-6Al-4V.

*Keywords:* Additive Manufacturing, Ti-6Al-4V, Powder Reuse, Tensile Properties, Oxidation

---

\*Corresponding author

*Email address:* nicholas.derimow@nist.gov (Nicholas Derimow<sup>1</sup>)

## 1. Introduction

Powder-bed fusion (PBF; -EB for electron beam, -L for laser) additive manufacturing (AM) often relies on reusing powder feedstock that has been collected from the build chamber post-build in order to maximize process efficiency. A recent review by Derimow and Hrabe [1] cataloged the different powder reuse methodologies that have been described in the literature for PBF of titanium alloy (Ti-6Al-4V). It is common industrial practice to mix unmelted powder from the build area with powder that never left the feed area after a given build. In PBF-EB, unmelted Ti-6Al-4V in the build area is sintered due to the high background temperature from layer preheating. Recent work [1] has even shown that oxidation is not consistent within a single build area, and was found to decrease with increasing build height. Therefore, the build area powder has higher oxygen content compared to the feed area powder. As oxygen content increases over many reuse events, eventually it no longer conforms to either ASTM F3001-14 [2] (0.013 wt.% O for Grade 23 Ti) or ASTM F2924-14 [3] (0.20 wt.% O for Grade 5 Ti). At this point, it is common industrial practice to mix in virgin, unused powder from the same lot to reduce the overall oxygen content and enable continued use of the newly mixed powder batch. For any mixing event, rule of mixtures (weighted mean) is assumed in calculating the new oxygen content. There have been several studies on PBF-EB Ti-6Al-4V regarding the effect of powder reuse on powder characteristics and properties [4–9], chemistry variations [10, 11], Charpy impact toughness [12], microstructure [6, 8, 13], and fracture properties [14]. However, none of them consider the possibility of oxygen content variation within a build.

We hypothesize that using rule of mixtures and assuming homogeneous mixing and oxygen content, when mixing two batches of powder with dissimilar oxygen content, is inappropriate, regardless of the mixing technique [15]. Along with differences in the oxidation, the flowability, sphericity, and humidity of the powder can also be affected based on reuse times, which therefore also affects the build process [16, 17].

We further hypothesize that localized oxygen content variation in mixed and heavily reused PBF-EB Ti-6Al-4V powder batches leads to significant variation in tensile properties for solid material built using these powders. In Ti-6Al-4V, small increases in oxygen content lead to large increases in tensile properties [16–18]. While increased strength can sometimes be a desirable outcome, uncontrolled changes in strength are undesirable as it can lead to unpredictable part performance. The present investigation builds on the conclusions from Part 1 [19] of this series, where there was a significant decrease in tensile yield strength with increasing build height. One of the contributing factors to this decrease in tensile strength was hypothesized to be related to a small decrease in oxygen content as the build progresses[1], likely due to the powder-bed scavenging O from the atmosphere at the beginning stages of the build [19].

This work seeks to explore the effect of powder mixing on this height-dependent tensile behavior, potentially leading to more stochastic variations in tensile strength than is observed in single-use powder builds. This was accomplished through testing material from a single build of PBF-EB Ti-6Al-4V using a mixed and heavily reused, yet ASTM F2924-14 [3] conforming, powder batch. High-throughput tensile testing of mini-tensile specimens has previously been utilized to study rare failure-critical defects [20] and stochastic tensile behavior [21] in additively manufactured 17-4PH stainless steel. In this work, 375 miniaturized tensile specimens were tested in a high-throughput manner, built across the entire build plate covering significant build height. We will systematically evaluate potential causes of variability in tensile properties, including porosity, microstructure, and chemistry to deduce the probable causes.

## 2. Methods

### 2.1. Build details

The powder feedstock consisted of 30 kg of reused Ti-6Al-4V powder measuring at 0.189 wt.% O that had been mixed with 20 kg of 0.080 wt.% O virgin powder to bring the average oxygen concentration down (rule of mixtures theoretical oxygen concentration = 0.145 wt.% O). The powder batch was mixed in a drum mixer with paddle inserts for 40 min at 1/3 volume capacity. The PBF-EB process was carried out on an Arcam A1<sup>1</sup> machine with standard Ti-6Al-4V build theme and layer height of 70  $\mu\text{m}$  (software version 3.2.132). The powder recoater direction was side-to-side relative to the front of the machine. The build layout is presented in Fig. 1a–b, where five groupings of three, vertically oriented 10 mm  $\times$  20 mm  $\times$  54 mm blocks (Fig. 1c) were spaced at the corners of the build plate, as well as in the center. There were 5 horizontal blocks built adjacent to each grouping, however these were used for bulk chemical analysis and not mechanically tested. The 15 vertical blocks were then machined into high-throughput tensile *racks*, each of which containing 25 mini-tensile coupons attached to a base (pictured in Fig. 1d) with gauge dimensions of 1 mm  $\times$  1 mm  $\times$  4 mm. In total, there were 15 racks of 25 numbered tensile coupons. Traceability was maintained, such that any given rack’s number 1 coupon corresponded to the top of the build.

### 2.2. Tensile testing

The specimens were tested at a displacement rate of 0.05 mm/s and strain rate of  $1.25 \times 10^{-2} \text{ s}^{-1}$  using a load frame with a 2000 lbf (8.896 kN) load cell (s/n: 555436A). A linear variable differential transformer

---

<sup>1</sup>Commercial names are identified in order to specify the experimental procedure adequately. Such identification is not intended to imply recommendation or endorsement by NIST nor does it imply that they are necessarily the best available for the purpose.

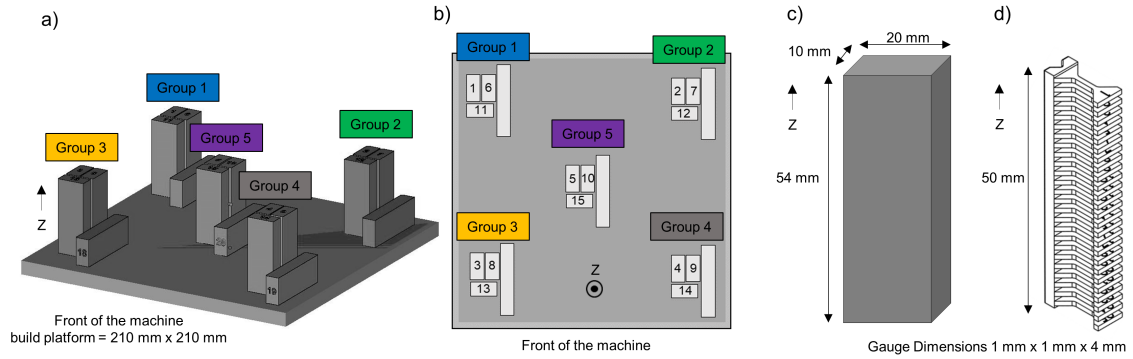


Figure 1: Build layout and subsequent rack machining diagram. a) Color coded group numbers pertain to location on the build plate. There were three blocks per group. Horizontal blocks were used for bulk solid chemistry analysis. b) Rack numbering per group c) Dimensions of the as-built block in each group, d) High-throughput tensile rack post-machining. Rack position ‘1’ corresponds to the top of the build (maximum Z-height/top of the build).

(LVDT) was used to guide load frame movement of the high-throughput setup. Two cameras (90 fps, 4.1 MPix) were used to capture images of samples during testing. During testing, a frame rate of 45 fps was used. The camera that captured images from the front of each tensile sample had a  $0.5\times$  lens attachment with  $12\times$  zoom and a  $1\times$  adapter. The camera that computed strain from images on the side of each tensile sample had no lens attachment with a  $12\times$  zoom and a  $2\times$  adapter. Three sets of LED lights with non-polarized white light with maximum intensity were used for illumination during digital image correlation (DIC). Each rack was initially painted with white spray paint. After the white paint dried, a thin, even coating of black spray paint was applied. As such, the pattern consisted of black speckles and white gaps. A typical speckle was about 12 pixels wide and a typical gap was about 6 pixels wide. The field-of-view to pixel ratio was  $1.93\ \mu\text{m}/\text{pixel}$ . Strain was computed using VicGauge2D and measured by a virtual extensometer with a length of 1.56 mm (810 pixels) using two gauges (subsets) of 89 pixels by 89 pixels. Engineering strain was used.

### 2.3. Characterization progression

In order to investigate any other contributing effects to tensile properties, the 375 tensile test specimens were down-selected for characterization. Fig. 2 demonstrates the selection process from the 375 tests down to 30 for microstructure, fractography, and bulk chemistry. These 30 specimens were of the 10 low, 10 medium, and 10 high yield strength (YS) specimens. These were down-selected further for electron backscatter diffraction (EBSD), where one specimen each from all five groupings were represented, while maintaining a sampling of 2 low YS, 1 medium YS, and 2 high YS specimens. Two low and two high YS specimens were chosen for micro X-ray computed tomography ( $\mu\text{XCT}$ ), while the lowest measured YS specimen and highest

measured YS specimen were chosen for time-of-flight secondary ion mass spectrometry (ToF-SIMS).

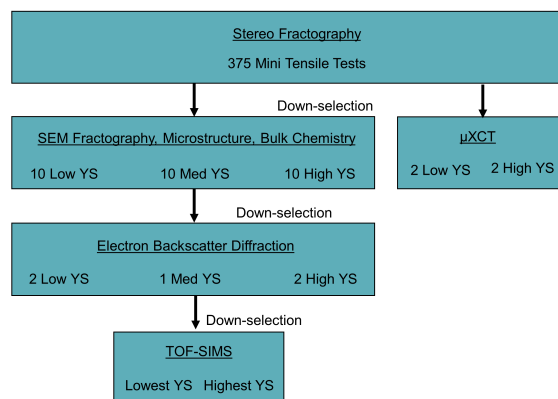


Figure 2: Flowchart detailing the down-selection of fractured specimens for characterization. The  $\mu$ XCT specimens were chosen separately from the microstructural and ToF-SIMS specimens.

#### 2.4. Fracture surface and internal porosity

The fractured surfaces of the tensile test specimens were imaged via stereoscopic microscopy and scanning electron microscopy. Micro X-ray computed tomography ( $\mu$ XCT) [22, 23] was utilized for volumetric data of the surface features and interior pores. Representative low and high yield strength tested tensile specimens were chosen for  $\mu$ XCT. For the  $\mu$ XCT measurements, the X-ray source and detector distances were chosen such that the specified voxel edge length was  $1.5 \mu\text{m}/\text{voxel} \pm 0.03 \mu\text{m}/\text{voxel}$ . A filter was used to reduce low-energy X-rays which cause beam hardening artifacts. The X-ray source power and detector exposure time were optimized on a per specimen basis to minimize scan time, while ensuring high quality reconstructions.

The tested specimens were rotated  $360^\circ$  about their long axis, during which time 1601 X-ray radiographs were captured. The reconstructed data were then saved as an image sequence (also commonly referred to as a TIFF stack) comprising 990 image-slices. Each resultant grayscale (16-bit) image-slice was 984 pixels in height and 1009 pixels in width. The grayscale images were then binarized using global thresholding techniques and quantitative image processing methods were applied to measure the porosity.

#### 2.5. Bulk chemistry, microstructure, and fractography

Bulk chemical analysis was carried out on an unused block of material from the build plate (similar to what is pictured in Fig. 1). Aluminum, vanadium, and iron were measured by optical emission spectroscopy (OES) per ASTM E2371-13 [24]. Oxygen and nitrogen were measured per ASTM E1409-13 [25], and hydrogen per ASTM E1447-09 [26], all by inert gas fusion. Carbon was measured by the combustion method per ASTM E1941-10 [27]. These values are presented in Table 1. The fractured halves of the 30

down-selected specimens were abraded to remove any wire EDM recast layer, cut to pieces, and tested for oxygen via inert gas fusion.

Table 1: Chemical composition in weight % of the the ASTM F2924-14 (Grade 5) limits and bulk/average measurements for the built material in this work.

Elem.	F2924-14	Solid chemistry
Al	5.5<x<6.75	5.76
V	3.5<x<4.5	4.16
Fe	0.30	0.28
O	0.20	0.17
C	0.080	0.011
N	0.050	0.038
H	0.0150	0.0018
Ti	bal.	bal.

Microscopy specimens of the fractured pieces were mounted in a conductive phenolic resin powder, abraded, and polished with 1  $\mu\text{m}$  diamond suspension. The mounted samples were then vibratory polished for approximately 24 h in 0.05  $\mu\text{m}$  colloidal silica. The microstructures were imaged using a field emission scanning electron microscope (FE-SEM) equipped with a Robinson backscattered electron (BSE) detector at an accelerating voltage of 20 kV. Crystallographic information was obtained via electron backscatter diffraction (EBSD) on the same SEM using an EBSD detector at an accelerating voltage of 20 kV and 1  $\mu\text{m}$  step size. Fractography was performed on the fractured halves of the specimens still attached in the high-throughput rack. The accelerating voltage for the fractography was 30 kV.

### 2.6. Time-of-flight secondary ion mass spectrometry

Time-of-flight secondary ion mass spectrometry (TOF-SIMS) was carried out on an IonTof TOF.SIMS 5 instrument. The primary ion beam was a three-lens BiMn cluster ion gun at 30 keV. The secondary ion beam used for sputtering was an oxygen electron impact gas ion source. An extended dynamic range analyzer was used to capture normally saturated signals to prevent data loss.

The primary ions were  $\text{Bi}^{3+}$  at 30 keV with a 70  $\mu\text{m} \times 70 \mu\text{m}$  field of view (FOV), outlined as a red box in Fig. 3, pixels = 128  $\times$  128 with a sawtooth raster mode and cycle time of 100  $\mu\text{s}$ . The eFlood gun was on. The sputter source was 2 eV  $\text{Cs}^+$  ( $\text{MCs}^+$ ) with a crater size of 250  $\mu\text{m} \times 250 \mu\text{m}$  (pictured as a blue box in Fig. 3). The sputtering conditions were interlaced.  $\text{MCs}^+$  mode is where Cs is run in positive mode, so examination of both positive and negative ions can be conducted in the same profiles. This also helps mitigate any matrix effects that commonly occur on metal oxide surfaces and layer interfaces. Three pits were sputtered into each of the tested specimens.

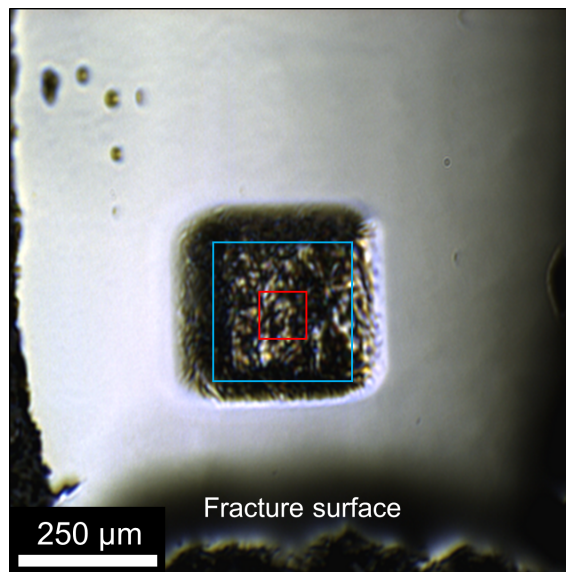


Figure 3: Optical micrograph of an example sputtering pit on the metallographically polished fractured surface. The blue square is the sputtering area, whereas the red box corresponds to the area of analysis.

### 3. Results

#### 3.1. Tensile properties

Each of the racks was tested such that all 25 mini tensile coupons per rack were brought to fracture. A summary of the tensile properties are presented in Fig. 4, with black horizontal data markers indicating the median value for each tensile rack. Fig. 5 displays a scatter plot of the UTS data versus elongation at fracture for all 375 tests. The data markers are color coded to match the grouping from where they came. Across the entire range of tensile tests, there was a spread of 138.9 MPa in YS and 156.3 MPa across the 375 tests, and the percent elongation at fracture ranged from 6.1 % to 17.2 %, and elastic modulus from 108.2 GPa to 129.4 GPa. Elastic modulus values are consistent with recent literature data of PBF-EB Ti-6Al-4V [28, 29]. Within the scope of the present investigation, however, the primary focus will be yield strength. The 138.9 MPa, or approximately 14 % difference, exists for the YS from the lowest YS specimen (972.8 MPa, referred to as L1) when compared to the highest YS specimen (1111.7 MPa, referred to as H10). The middle YS specimen of 1028.9 MPa is referred to as M7. The lowest, middle, and highest YS specimens' engineering stress-strain curves are plotted in Fig. 6 to illustrate the extrema of the test specimens' tensile properties. The sharp dip in Fig. 6 around 2 % strain is a post-yield unloading/reloading intentionally included for a more accurate measurement of elastic modulus.

As every tensile test was traceable back to the build height on the high-throughput tensile rack, the YS for each test was plotted against the build height (in mm) for each rack, as presented in Fig. 7. All

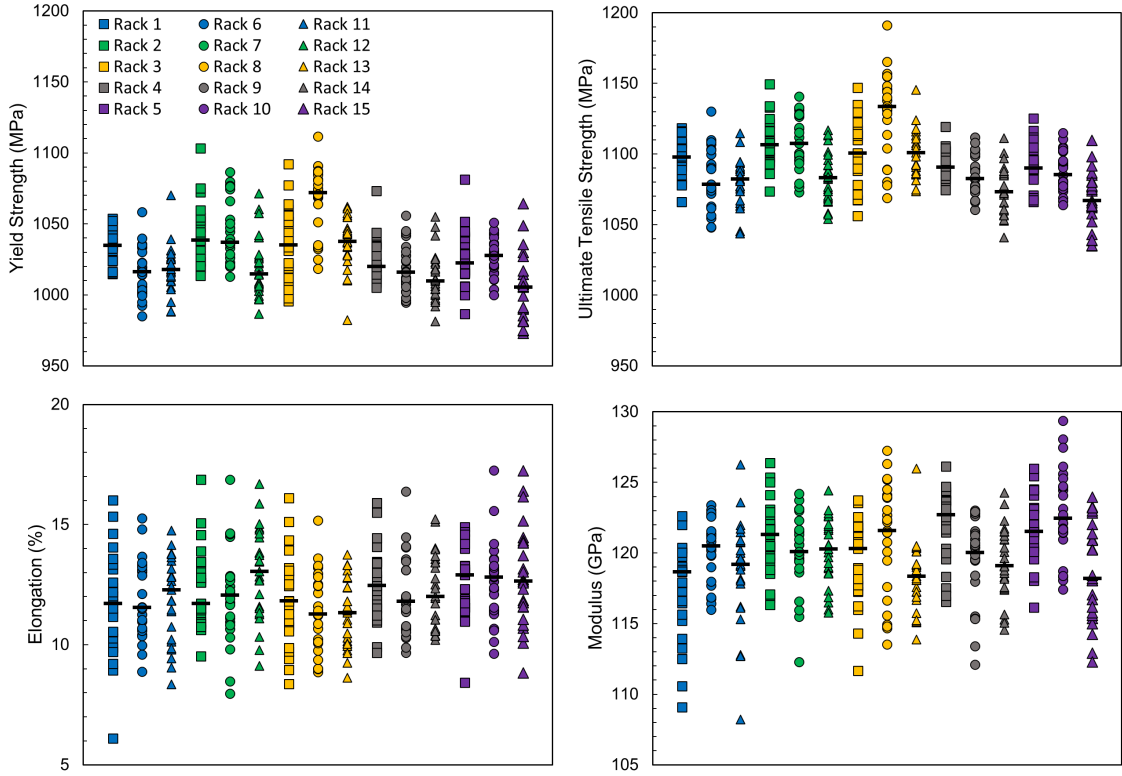


Figure 4: Summary of tensile properties. Horizontal black markers indicate median values for each rack.

375 tensile tests are plotted in Fig. 7, with the color coding of the data markers indicating the location on the build plate where the tensile rack was built. Linear regression trendlines are added as straight dotted lines through the data sets. All racks except Rack 6 and Rack 8 show negative sloping linear regressions, indicating that YS decreased with the increase of build height. The  $R^2$  values for the linear regressions are presented in Table 2.

### 3.2. Porosity

Stereo light fractography was carried out on all 375 tensile specimens in order to screen any potential killer defects that could result in any abnormal tensile behavior. Since no correlation between YS and fracture surface porosity was observed, 10 low YS, 10 medium YS, and 10 high YS specimens were down-selected as representative tests that covered the extrema in YS values. These 30 specimens were given unique identifiers, and are located in Table 3 along with material properties such as YS, UTS, elastic modulus (E), elongation at fracture, inert gas fusion oxygen measurements, and  $\alpha$ -lath thickness measurements, the latter two of which will be discussed in the subsequent sections.

For the lowest (L1), medium (M7), and highest (H10) YS specimens, secondary electron (SE) based

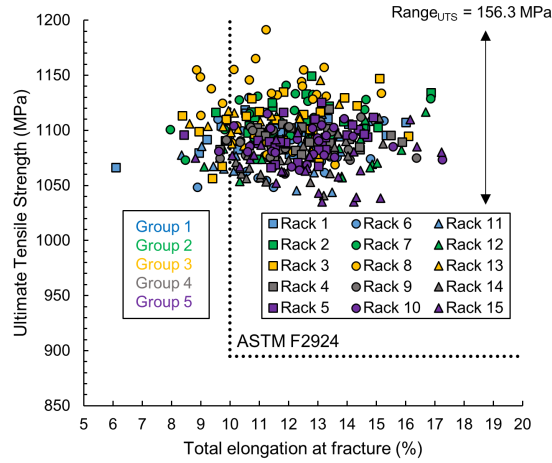


Figure 5: Ashby scatter plot of the UTS versus percent total elongation. The  $\text{Range}_{\text{UTS}}$  label corresponds to the total range of UTS values measured across all tests.

Table 2: Linear regression  $R^2$  values (%) for the YS versus build height plots for Racks 1–15.

Group	Rack	$R^2$ (%)
1	1	5.09
2	2	50.14
3	3	45.28
4	4	29.61
5	5	36.87
1	6	7.07
2	7	36.37
3	8	1.02
4	9	48.69
5	10	4.04
1	11	28.62
2	12	25.63
3	13	16.50
4	14	17.28
5	15	68.33

fractography was carried out in order to resolve the fracture surfaces in greater detail. The fractographs are presented in Fig. 8, where Fig. 8a–c correspond to specimens L1, M7, and H10, respectively. The fractured surfaces exhibited typical microvoid coalescence morphology. The white arrows in Fig. 8 indicate fracture surface porosity. The shape of the porosity for all the specimens was generally spherical, in the size range of approximately 10  $\mu\text{m}$  to 70  $\mu\text{m}$ .

In order to exclude the possibility of unusual porosity in low and high strength specimens that would unduly affect,  $\mu\text{XCT}$  was employed to measure the internal void volumes close to the fracture surface of four fractured tensile specimens. Fig. 9 displays two low YS (Fig. 9a–b) and two high YS (Fig. 9c–d) broken test pieces, with highlighted void volumes in red. The reconstructed specimens in Fig. 9a–b were taken from

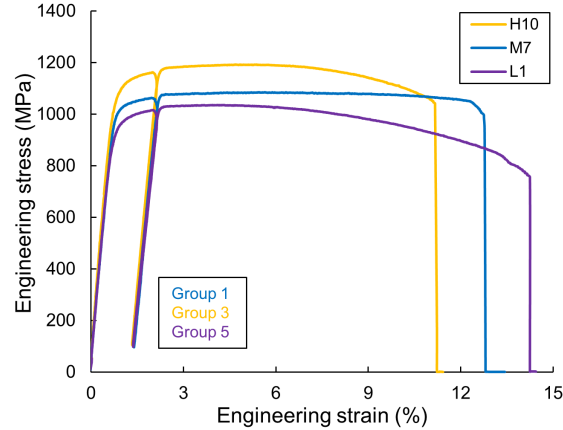


Figure 6: Engineering stress-strain curves for the lowest YS (L1), medium YS (M7), and highest YS specimen (H10). Colors correspond to grouping on the build plate. The sharp lines after yield indicate a deliberate post-yield unloading/reloading sequence.

Rack 15 at  $Z = 28$  mm (YS = 981.2 MPa) and  $Z = 38$  mm (YS = 991.2 MPa), respectively. The specimen in Fig. 9c was taken from Rack 8 at  $Z = 44$  mm (1086.5 MPa), while Fig. 9d was taken from Rack 7 at  $Z = 6$  mm (1079.8 MPa). The total averaged porosity for the low YS specimens was 0.056 vol.%, whereas the high YS specimens were measured to have 0.136 vol.% porosity.

### 3.3. Microstructure

The microstructure of the 30 down-selected specimens L1–L10, M1–M10, and H1–H10 were analyzed via BSE in order to measure the average  $\alpha$ -lath thicknesses for each of the as-built microstructures in the gauge section, outside the plastically deformed necked region. The average  $\alpha$ -lath thickness for all 30 specimens are reported in Table 3. Each measurement represents 50 individual  $\alpha$ -lath measurements with  $1\sigma$  standard deviation. Representative BSE images were chosen to represent each low, medium, and high YS grouping (L1, M7, and H10). The microstructures for the L1, M7, and H10 specimens are shown in Fig. 10. The morphology of each specimen consisted of  $\alpha/\beta$  Widmännstätten, or basket-weave microstructure, with darker colored regions representing hexagonal closed packed  $\alpha$  phase, while the brighter constrained regions consist of body-centered cubic  $\beta$  phase. The  $\alpha$ -lath thicknesses for L1, M7, and H10 in Fig. 10 were measured to be  $0.88 \mu\text{m} \pm 0.20 \mu\text{m}$ ,  $0.87 \mu\text{m} \pm 0.25 \mu\text{m}$ , and  $0.97 \mu\text{m} \pm 0.30 \mu\text{m}$ , respectively.

Crystallographic analysis was carried out on further down-selected specimens from the 30 microstructural samples. The EBSD specimens were carefully chosen to represent two low (L1, L4), one medium (M7), and two high (H9, H10) YS tests. These five specimens also represent all of the groups on the build plate (Group 1 = M7, Group 2 = H9, Group 3 = H10, Group 4 = L4, and Group 5 = L1). This was done to investigate

Table 3: Summary of material properties for the 30 down-selected specimens chosen for microstructural and chemical analysis. H = height, YS = yield strength, UTS = ultimate tensile strength, E = elastic modulus, El. = elongation. Oxygen chemistry in wt.% is bulk chemistry of the bottom half of the fractured tensile specimen, cut from the machined rack and measured with LECO.  $\alpha$  lath refers to 60 averaged  $\alpha$  laths measured from the microstructure for each of the specimens.

ID	Group	Rack	H (mm)	YS (MPa)	UTS (MPa)	E (GPa)	El. %	wt.% O	$\alpha$ -lath ( $\mu\text{m}$ )
L1	5	15	36	972.8	1035.0	112.3	14.2	0.171	$0.88 \pm 0.20$
L2	5	15	34	974.7	1038.6	116.7	15.2	0.181	$0.97 \pm 0.27$
L3	5	15	32	975.0	1035.2	114.3	13.2	0.183	$1.04 \pm 0.33$
L4	4	14	36	981.2	1040.9	118.3	13.2	0.176	$0.88 \pm 0.25$
L5	1	6	22	985.1	1048.3	116.9	11.5	0.186	$0.90 \pm 0.28$
L6	2	12	32	986.6	1058.0	119.0	13.8	0.180	$0.87 \pm 0.22$
L7	1	11	42	988.1	1045.3	108.2	12.3	0.181	$0.97 \pm 0.24$
L8	4	14	40	988.5	1043.7	116.2	13.5	0.184	$0.82 \pm 0.31$
L9	4	14	48	991.9	1060.5	120.9	10.4	0.181	$0.73 \pm 0.22$
L10	1	6	24	992.4	1048.2	116.4	8.9	0.180	$1.01 \pm 0.32$
M1	4	9	36	1027.7	1102.9	122.6	10.7	0.184	$0.85 \pm 0.30$
M2	5	10	8	1027.7	1085.0	124.4	15.6	0.206	$0.89 \pm 0.27$
M3	5	10	28	1027.8	1080.8	121.0	11.4	0.182	$0.91 \pm 0.31$
M4	5	10	50	1027.8	1095.4	121.7	13.3	0.174	$0.85 \pm 0.24$
M5	5	5	12	1028.5	1089.5	124.5	11.7	0.186	$0.99 \pm 0.31$
M6	2	7	16	1028.7	1093.5	119.9	10.8	0.185	$0.96 \pm 0.25$
M7	1	11	4	1028.9	1084.3	120.9	12.8	0.186	$0.87 \pm 0.25$
M8	5	10	42	1029.3	1090.4	118.1	13.0	0.180	$0.96 \pm 0.40$
M9	1	6	40	1030.2	1108.5	122.7	15.3	0.202	$0.92 \pm 0.30$
M10	1	1	12	1030.5	1097.9	119.0	11.7	0.196	$1.00 \pm 0.41$
H1	2	7	8	1077.4	1132.6	121.0	12.8	0.194	$0.80 \pm 0.23$
H2	5	5	2	1081.4	1125.2	122.7	13.1	0.196	$0.77 \pm 0.22$
H3	3	8	38	1084.8	1154.9	121.6	12.5	0.206	$0.98 \pm 0.25$
H4	2	7	10	1086.4	1140.9	120.1	11.9	0.189	$0.78 \pm 0.25$
H5	3	8	16	1086.8	1155.2	124.1	10.1	0.170	$0.86 \pm 0.26$
H6	3	8	18	1087.4	1144.3	121.5	12.5	0.175	$0.82 \pm 0.25$
H7	3	8	42	1090.8	1165.3	122.7	10.9	0.166	$0.78 \pm 0.26$
H8	3	3	4	1092.0	1146.9	123.7	15.1	0.174	$0.76 \pm 0.23$
H9	2	2	2	1103.4	1149.4	126.4	12.8	0.191	$0.71 \pm 0.22$
H10	3	8	48	1111.7	1191.3	127.2	11.2	0.141	$0.97 \pm 0.30$

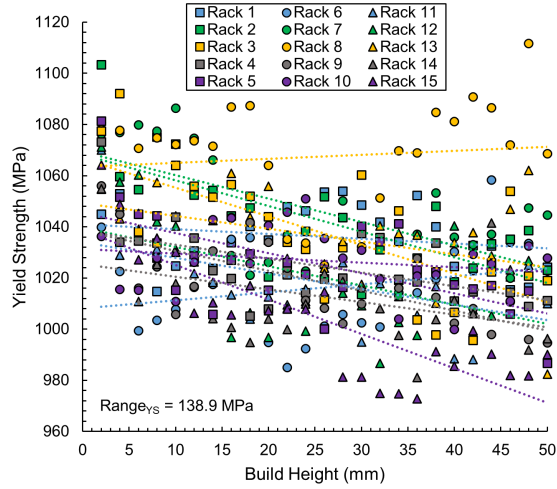


Figure 7: Build height versus yield strength for each of the blocks. Color coded trend lines are linear regression fits for each of the blocks.  $\text{Range}_{\text{YS}}$  = total range of YS values across all tests.

if crystallographic texture differences from the location on the build plate contributed to the YS variation between low and high YS specimens. Fig. 11 displays an inverse pole figure (IPF) map (parallel to the build direction in Z) for each of the five specimens representing their group on the build plate. Immediately to the right of the IPF maps are pole figures for the  $\langle 0001 \rangle_{\alpha}$  and  $\langle 11\bar{2}0 \rangle_{\alpha}$  directions, which all show the same relatively weak texture character in the  $\langle 11\bar{2}0 \rangle_{\alpha}$  direction, oriented in the Z direction.

### 3.4. Chemistry

The 30 down-selected microstructure specimens consisted of one half of the fractured test piece. As those were mounted in phenolic resin for microstructural analysis, the remaining halves of the tensile specimens, including gauge section material as well as grip material, were abraded to remove any wire-EDM recast layer, broken into pieces, and were tested for oxygen content via inert gas fusion. The wt.% O values for all 30 fractured halves is reported in Table 3, and visualized as mean values in Fig. 12. The mean values for the oxygen content all conform to ASTM F2924-14 [3]. The high YS specimens had the largest amount of scatter in oxygen concentration.

### 3.5. ToF-SIMS

Time-of-flight secondary ion mass spectrometry (ToF-SIMS) was carried out on the lowest YS (L1) and highest YS (H10) specimens in gauge section areas near the fractured surface (Fig. 3) in order to approximate relative oxygen content differences between the two samples. The metallographically polished and mounted pieces were inserted directly into the ToF-SIMS device as the bakelite puck dimensions fit inside of the test

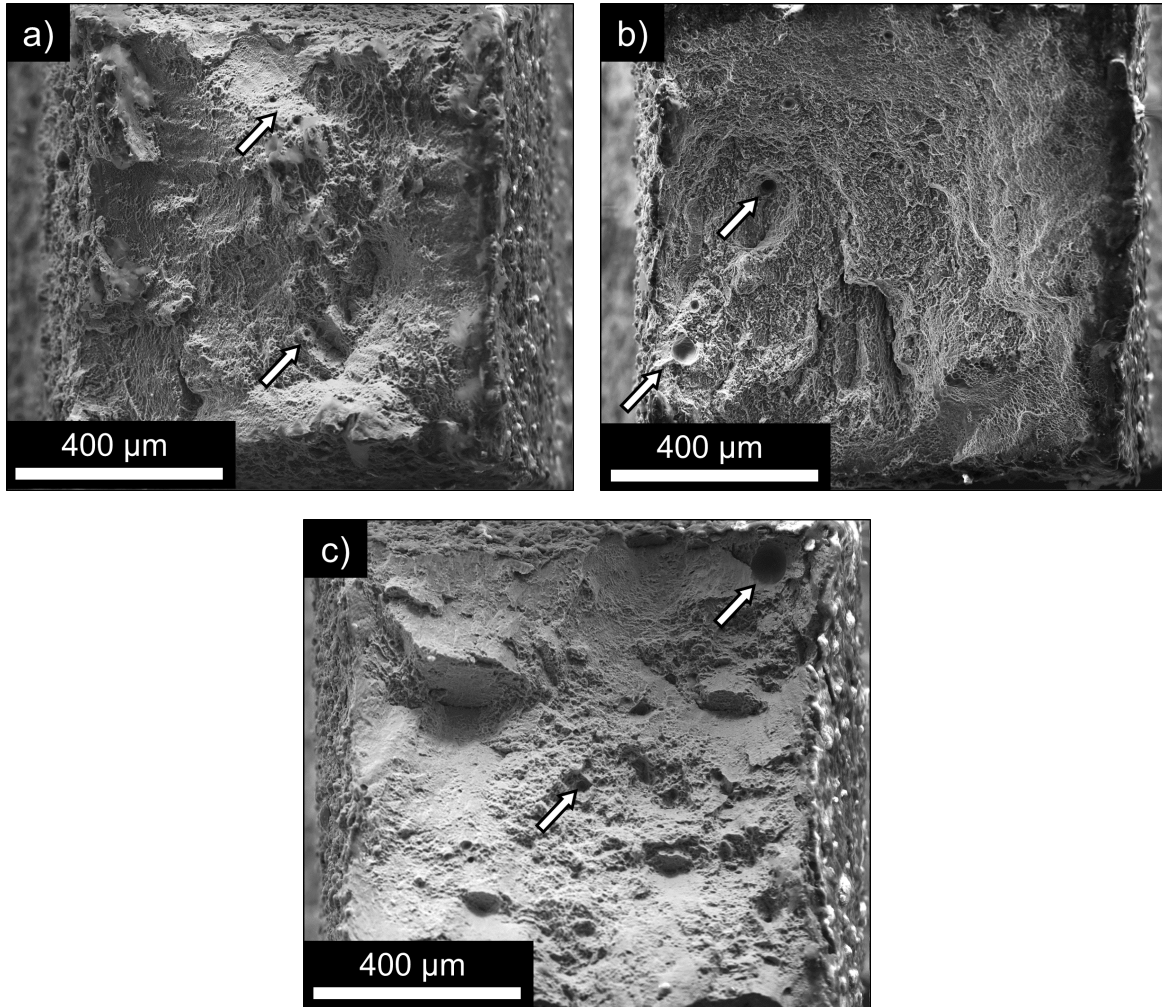


Figure 8: Fractography of the a) lowest YS specimen (L1), b) medium YS specimen (M7), and c) highest YS specimen (H10). White arrows point to surface porosity.

chamber. The sputtering pits ranged from approximately  $0.7 \mu\text{m}$  to  $3.5 \mu\text{m}$  across the six measurements. The ion counts were gathered over equal time frames, and the % relative  $\text{Cs}_2\text{O}^+$  and  $\text{CsTi}^+$  ions to total ions were normalized for each of the sputtering pits per unit time and presented as a function of time in Fig. 13.

The first few layers of sputtering initially removed the nanometers-thick native oxide layer of the Ti-6Al-4V alloy, followed by continuous sputtering into the alloy for 1000 s. The data presented in Fig. 13 has been smoothed using 50 point averaging in the x-axis. Fig. 14 displays only the  $\text{Cs}_2\text{O}^+$  ions for the low YS (green) and high YS (blue) sputtering pits. The three sputtering pits for the high YS specimen contained consistently higher oxygen ions when normalized to the total ion count for those given pits as a function of

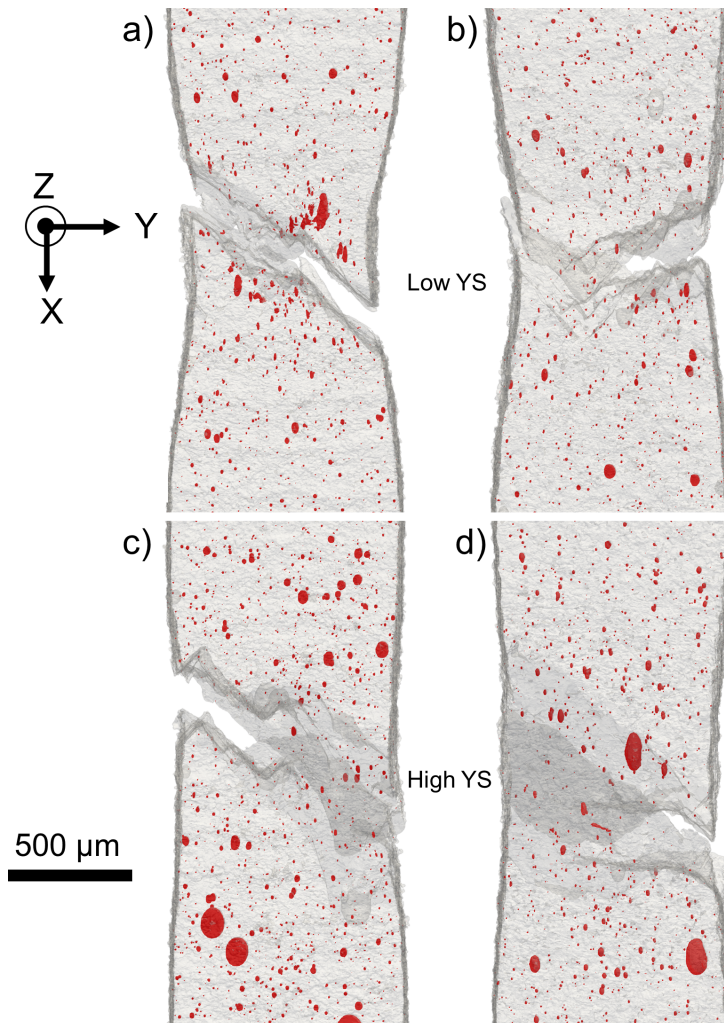


Figure 9: Digital rendering of the pores in red in the gauge sections of a-b) two low YS specimens and c-d) two high YS specimens. Z = build direction, X = loading/tensile direction.

time when compared to the low YS pits.

#### 4. Discussion

The tensile properties for the 375 mini tensile specimens presented in the histogram in Fig. 4 display statistically significant differences between the rack tensile measurements. Mixing of reused powder is one simple possible cause for the wide range of values, however pinpointing the underlying structure-property relationship causality for this wide distribution requires more scrutiny. The observations made in Part 1 [19] of this 2-part paper series indicated that there is a height dependence of the YS for Ti6-Al-4V produced with virgin feedstock. That is, as height increases, YS decreases linearly. The cause of this effect was deduced

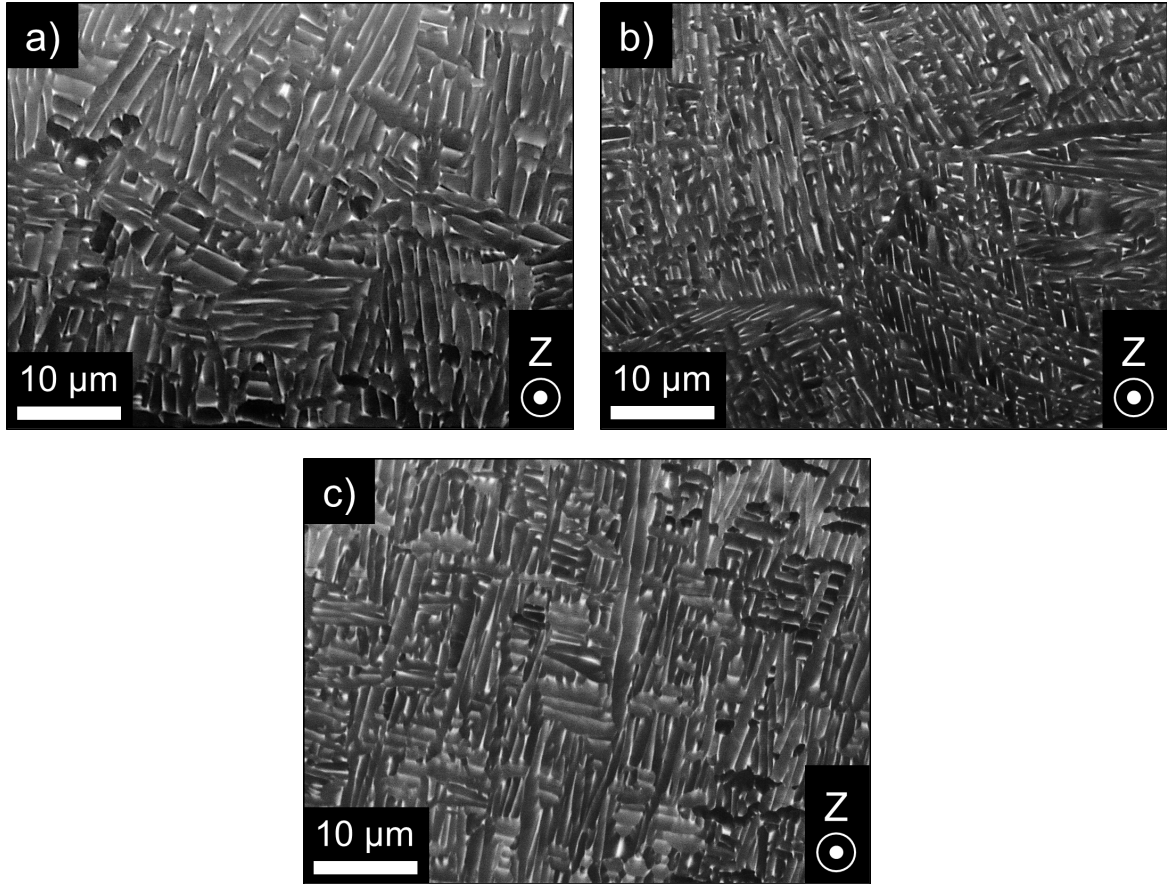


Figure 10: BSE image of the microstructure of the a) lowest YS specimen (L1), b) medium YS specimen (M7), and c) highest YS specimen (H10). Z = build direction.

to be likely oxygen (and possibly other elemental) changes from the beginning layers of the build due to the high background processing temperature inherent to PBF-EB and transient sources of oxygen present at the beginning of the build. Similar to the investigation into the extreme-value statistics of failure-critical defects in PBF-L 17-4 PH stainless steel [20], the goal of this work is to investigate the cause for outliers in tensile performance to mitigate heterogeneous material behavior in AM production environments. It is common practice to blend reused, higher oxygen content Ti-6Al-4V powder with either low oxygen content, or virgin powder to bring down the average oxygen concentration (as measured by inert gas fusion) of the entire batch.

Comparing the YS versus build height data (Fig. 7) for the high-throughput tensile racks used in this work to the virgin blocks in Part 1 [19] is not as straightforward. The  $R^2$  values for the linear regression fits in Part 1 ranged from 67.15 % to 84.77 %, whereas the  $R^2$  values for the linear regressions for build height in this work are much more variable (Table 2). However, no one rack displays the full range of variation, and

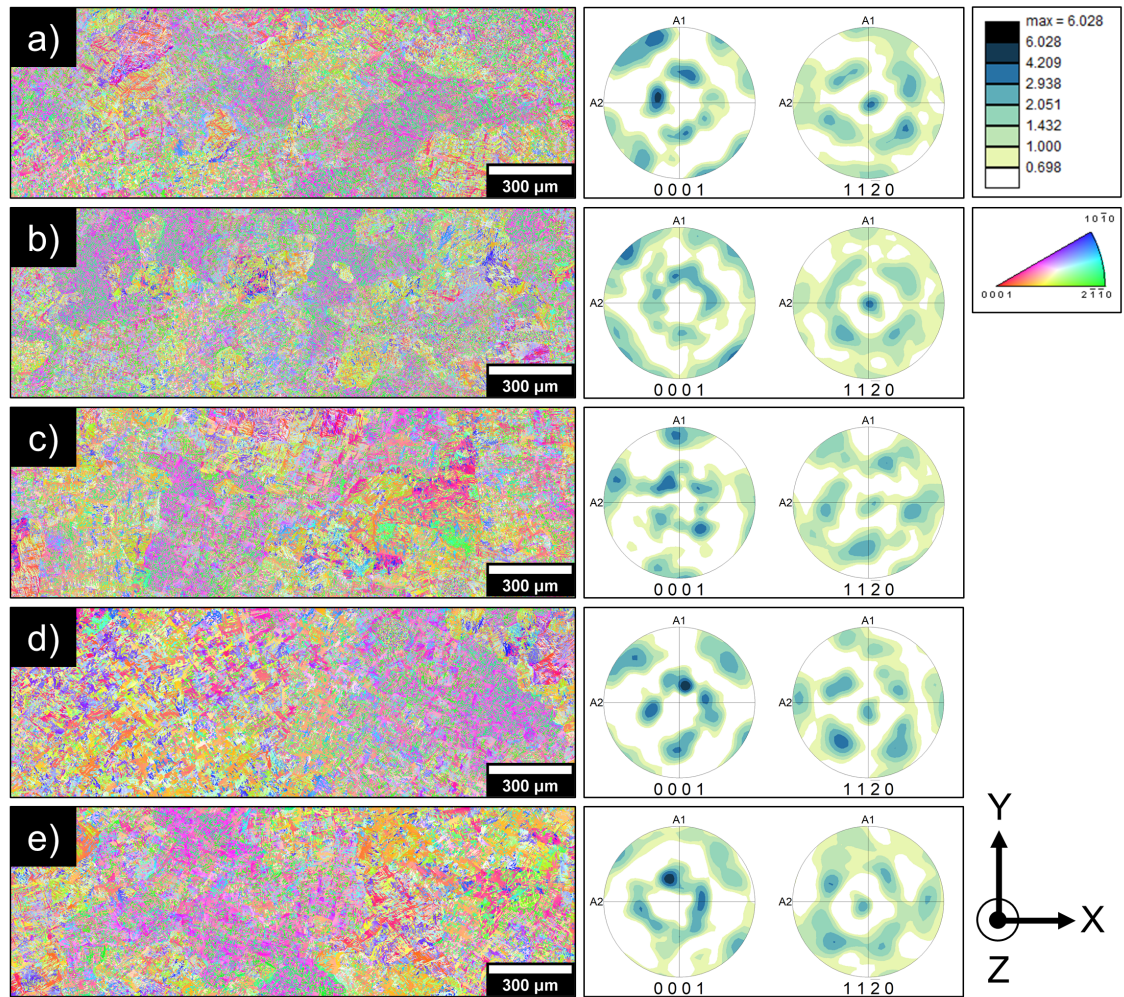


Figure 11: Electron backscatter diffraction (EBSD) of 5 group locations on the build plate. Pole figures for the corresponding IPF map are located on the right. 1) Group 1 (M7), b) Group 2 (H9), c) Group 3 (H10), d) Group 4 (L4), and e) Group 5 (L1). Z = build direction, X = loading/tensile direction. The IPF maps are oriented in [001], such that the poles are parallel to the build direction (Z). Pole figure heat map corresponds to multiples of random distribution (m.r.d.).

trends within racks vary between being somewhat build-height dependent (those with higher  $R^2$ , following the trends observed in [19]), and racks lacking such a dependency. This indicates that there are multiple contributions impacting YS, which we suppose may be related to powder mixing. Namely, the  $R^2$  values in this work range from essentially no fit (Racks 1, 6, 8, and 10  $\approx 1\%$  -  $7\%$ ) to reasonable correlation (Rack 15, 68.33%). The effect of the build height is not as clear, as could be a competing parameter that is affecting the YS in conjunction with build height. There were no obvious correlations between build plate location (Group) and tensile properties shown in Fig. 4.

All 375 fractured surfaces were investigated via light stereo microscopy, and we found no clear feature (severe surface porosity, change in fracture mechanism) that could explain the variation in YS. For example,

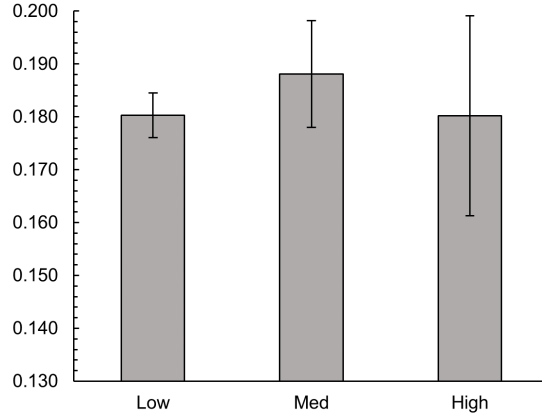


Figure 12: Bar chart summarizing the average oxygen content of the Low, Medium, and High YS specimens. Error bars represent  $1\sigma$ .

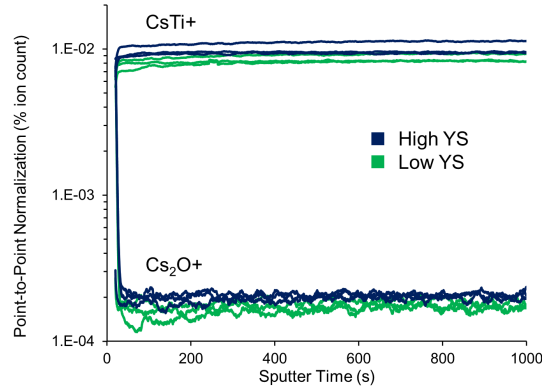


Figure 13: ToF-SIMS point-to-point normalization percent ion count for  $\text{CsTi}^+$  (top) and  $\text{Cs}_2\text{O}^+$  (bottom) ions as a function of sputtering time in seconds.

the lowest YS specimen, L1 (pictured in Fig. 8a) has small surface pores and typical microvoid coalescence fracture surface morphology, but nothing that sets it drastically apart from a medium YS (M7) or the highest YS (H10) specimens shown in Fig. 8b-c. The  $\mu\text{XCT}$  of two low YS (0.056 vol.% porosity) and two high YS (0.136 vol.% porosity) did not reveal porosity levels that could have contributed to such a wide variation in YS, as demonstrated by Shanbhag et al. [30]. The average porosity measured via  $\mu\text{XCT}$  in Part 1 of this series [19] for the low YS specimens was 0.1043 vol.%, while the high YS specimens were measured to be 0.06234 vol.%, which is an opposite to the correlation in the present work (low YS = 0.056 vol.%, high YS = 0.136 vol.%). Therefore, it is reasonable to assume that the measured porosity levels in these specimens are not contributing to the large variations in YS. These levels can be treated as the nominal range of expected as-built specimen porosity for the present conditions, and are subject to sampling volume

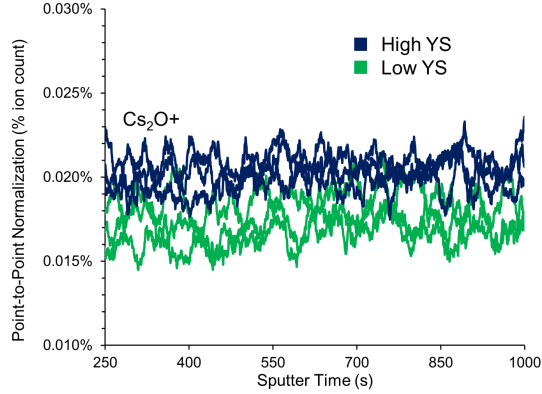


Figure 14: Portion of the  $\text{Cs}_2\text{O}^+$  ion counts from Fig. 13 from 250 s to 1000 s, illustrating the difference in total ion count for the lowest YS (L1) and highest YS (H10) specimens.

constraints that likely contribute substantially to the observed percentages (e.g., one or two random, large voids could account for a plurality of the measured void space in any example image).

The racks from each of the XY location groupings (Groups 1 – 5) all displayed similar, yet relatively weak  $\langle 11\bar{2}0 \rangle_\alpha$ , crystallographic texture character. The texture of the as-built material in this work is also the same texture observed in Part 1 [19]. Based on previous texture studies on PBF-EB Ti-6Al-4V [31], it is reasonable to assume that there was no texture dependence on build height, and that each of these groupings had the same  $\langle 11\bar{2}0 \rangle_\alpha$  texture character. The microstructure of the L1, M7, and H10 specimens shown in Fig. 10 is the typical  $\alpha/\beta$  Widmännstatten microstructure that is found in PBF-EB Ti-6Al-4V, and the same as those in Part 1 [19]. The  $\alpha$ -lath thickness for the specimens in this work ranged from 0.87  $\mu\text{m}$  to 0.97  $\mu\text{m}$ , and when compared to previous studies by Tiley et al. [32] and Kar et al. [33], should not correspond to 138.9 MPa in YS variation. The work by Ghamarian et al. [34] postulates the YS contributions from grain size effects and solid solution strengthening, concluding that solid solution strengthening is the major contributing factor to YS increases.

Interstitial oxygen solid solution strengthening in titanium alloys [18] is well understood, especially within the context of PBF AM [35]. Previous work by Derimow et al. characterized the sintered powder that was sampled from the powder bed at known Z-heights [1]. It was observed that oxidation preferentially occurred at the beginning of the build due to the high background processing temperatures paired with the natural gettering affinity of titanium to react with free oxygen in the environment. The authors showed in Part 1 [19] of this series that the YS decrease correlated to higher Z-height was in part due to higher oxygen content near the bottom of the build, which also decreased as the build got taller. For the present study, the inert gas fusion oxygen measurements were taken from all 30 L1 – L10, M1 – M10, and H1 – H10 specimens with

no special consideration for build height. Due to the much smaller gauge section dimensions used in the present investigation, much more material stemming from the grip section was used in order to get adequate sample sizes for the tests. Note that only one half of the fractured piece was used for inert gas fusion, as the other half was used for microscopy. The bulk material (pre-machining) chemistry analysis present in Table 1 shows the oxygen content being 0.17 wt.% O. This value is close to the inert gas fusion oxygen measurements for the 30 specimens presented in Fig. 12, however illustrates the stochastic variation present in chemical analysis of these tested specimens. The results from the 30 oxygen tests do not appear to correlate with the YS measurements. However, due to the amount of material needed to conduct a successful measurement, we could speculate that small, heterogeneous concentrations of oxygen in the mini-tensile bars were masked by the nature of the bulk measurement.

In order to further investigate the effects of oxygen, the lowest YS (L1) and highest YS (H10) specimens were investigated via ToF-SIMS such that areas near the fracture surfaces could be examined without completely destroying the sample. From the three sputtering pits chosen per sample near the fracture surfaces, there was consistently higher relative  $\text{Cs}_2\text{O}^+$  ions for the high YS specimen relative to the low YS specimen. These measurements were limited to the surface, but serve as an indication that oxygen may have had a role in influencing the local material properties in these alloys. There was also slightly less measured  $\text{CsTi}^+$  ion relative to the total ion counts measured for L1 when compared to H10 (Fig. 13). This may be due to other chemistry changes resulting from varying amounts of Al, V, or Fe content, and remains an open question. Ghamarian et al. [34] reported that changes in Al, V, and Fe can lead to changes in YS. However, the direct effects of such elements will be investigated in future work.

When comparing the spread in yield strength (138.9 MPa) in this work to the observed yield strength variation for the virgin build in Part 1 [19] of this series (74.2 MPa), it is evident that there are significant effects that arise from using reused/blended powder. The root causes remain to be fully understood, however it is reasonable to assume that the chemical heterogeneity on a per-particle basis seems to increase the potential for tensile performance variability in these materials. Future work will focus on the effects of different types of industrial mixing techniques (e.g. v-mixing) on intra-build oxygen content and tensile property variation. However, we feel it is likely that without sufficient driving force for mixing (e.g. particle size distribution changes), random mixing will never achieve true homogeneity. The authors suggest that in order to mitigate any unwanted changes in chemistry, powder quarantining, as described in the recent review by Derimow and Hrabec [35], may prove to be useful in maintaining similar chemistry among reused powder batches. For an example virgin build, this could potentially be achieved by quarantining a batch of powder

that has been through the AM machine once, until the entire lot has been through the machine the same number of times. Then the powder batch could be blended together, given that the entire quarantined lot would have been exposed to the machine the same number of times (provided that the builds are similar).

## 5. Conclusion

Heavily mixed and reused powder (30 kg) with high oxygen content was mixed with virgin Grade 23 Ti-6Al-4V ELI powder (20 kg) from the same lot to simulate a real world production environment powder blending operation. This was done in order to investigate the effect of powder mixing and reuse on tensile properties of parts coming from an electron beam powder-bed fusion build that utilizes reused and mixed feedstock powder. The following conclusions have been drawn from the present investigation:

- An approximate 139 MPa variation in yield strength was observed over the 375 mini tensile tests coming from the same build and sampling the entire build area and a build height of approximately 55 mm.
- The yield strength variation is attributable in some cases to build height dependence, since the higher yield strength tests came from specimens toward the bottom of the build (lower Z-height).
- The yield strength variation also occurs in part due to localized differences in chemistry of the specimens, indicating that there are simultaneous effects (build height + powder particles with varying chemistry) that can lead to a large spread in yield strength for areas within a given build.
- Effects of porosity, fracture surface features, microstructure, or crystallographic texture were not attributable to the yield strength differences for the specimens tested in this work. Indicating that in this particular case, the YS increases stemmed mostly from solid solution strengthening.
- Bulk oxygen measurements may not be sufficient for characterizing the localized oxygen concentrations at small length scales. One option that might reduce intra-build variability is powder quarantining to mitigate undesirable intra-build variations in chemistry and tensile properties.

## 6. Acknowledgments

This material makes use of the TOF-SIMS equipment at the Colorado School of Mines, which was supported by the National Science Foundation under Grant No.1726898. This research was performed while N. Derimow, N. Moser, and O. Kafka held National Research Council (NRC) Postdoctoral Research

Associateships at the National Institute of Standards and Technology (NIST). F. DelRio was supported by the Center for Integrated Nanotechnologies, a Department of Energy office of Basic Energy Sciences user facility. Sandia National Laboratories is a multimission laboratory managed and operated by National Technology & Engineering Solutions of Sandia, LLC, a wholly owned subsidiary of Honeywell International Inc., for the U.S. Department of Energy's National Nuclear Security Administration under contract DE-NA0003525. The authors wish to thank Brandon Hentges and Skye Stuckey of 3D Systems. The authors also would like to thank Enrico Lucon, Jordan Weaver, Nicholas Ritchie, Greg Gillen, and Ryan White at NIST.

## References

- [1] N. Derimow, A. Romero, A. Rubio, C. Terrazas, F. Medina, R. Wicker, N. Hrabec, [Sintered powder oxidation variation as a function of build height for titanium alloy produced by electron beam powder-bed fusion](#), Additive Manufacturing Letters 1 (2021) 100023. doi:10.1016/j.addlet.2021.100023.  
URL <https://doi.org/10.1016/j.addlet.2021.100023>
- [2] ASTM F3001-14, Standard Specification for Additive Manufacturing Titanium-6 Aluminum-4 Vanadium ELI (Extra Low Interstitial) with Powder Bed Fusion, ASTM Standards (2014) 1–6doi:10.1520/F3001-14.
- [3] ASTM F2924-14, Standard Specification for Additive Manufacturing Titanium-6 Aluminum-4 Vanadium with Powder Bed Fusion, ASTM Standards (2014). doi:10.1520/F2924-14.2.
- [4] A. Mohammadhosseini, D. Fraser, S. H. Masood, M. Jahedi, A Study of Morphology of Titanium Powder Used in Electron Beam Melting, Applied Mechanics and Materials 541-542 (2014) 160–163. doi:10.4028/www.scientific.net/AMM.541-542.160.
- [5] A. Strondl, O. Lyckfeldt, H. Brodin, U. Ackelid, Characterization and Control of Powder Properties for Additive Manufacturing, Jom 67 (3) (2015) 549–554. doi:10.1007/s11837-015-1304-0.
- [6] Y. Sun, M. Aindow, R. J. Hebert, [The effect of recycling on the oxygen distribution in Ti-6Al-4V powder for additive manufacturing](#), Materials at High Temperatures 35 (1-3) (2018) 217–224. doi:10.1080/09603409.2017.1389133.  
URL <http://doi.org/10.1080/09603409.2017.1389133>
- [7] G. Shanbhag, M. Vlasea, [The effect of reuse cycles on Ti-6Al-4V powder properties processed by electron beam powder bed fusion](#), Manufacturing Letters (2020). doi:10.1016/j.mfglet.2020.07.007.  
URL <https://doi.org/10.1016/j.mfglet.2020.07.007>
- [8] S. Ghods, E. Schultz, C. Wisdom, R. Schur, R. Pahuja, A. Montelione, D. Arola, M. Ramulu, [Electron Beam Additive Manufacturing of Ti6Al4V: Evolution of Powder Morphology and Part Microstructure with Powder Reuse](#), Materialia 9 (December 2019) (2020) 100631. doi:10.1016/j.mtla.2020.100631.  
URL <https://doi.org/10.1016/j.mtla.2020.100631>
- [9] A. Montelione, S. Ghods, R. Schur, C. Wisdom, D. Arola, M. Ramulu, [Powder Reuse in Electron Beam Melting Additive Manufacturing of Ti6Al4V: Particle Microstructure, Oxygen Content and Mechanical Properties](#), Additive Manufacturing 35 (December 2019) (2020) 101216. doi:10.1016/j.addma.2020.101216.  
URL <https://doi.org/10.1016/j.addma.2020.101216>

- [10] P. Nandwana, W. H. Peter, R. R. Dehoff, L. E. Lowe, M. M. Kirka, F. Medina, S. S. Babu, Recyclability Study on Inconel 718 and Ti-6Al-4V Powders for Use in Electron Beam Melting, *Metallurgical and Materials Transactions B* 47B (February) (2016) 754–762. doi:[10.1007/s10884-015-9497-z](https://doi.org/10.1007/s10884-015-9497-z).
- [11] Y. Cao, M. Delin, F. Kullenberg, L. Nyborg, Surface modification of Ti-6Al-4V powder during recycling in EBM process, *Surface and Interface Analysis* (May) (2020) 7–11. doi:[10.1002/sia.6847](https://doi.org/10.1002/sia.6847).
- [12] W. A. Grell, E. Solis-Ramos, E. Clark, E. Lucon, E. J. Garboczi, P. K. Predecki, Z. Loftus, M. Kumosa, [Effect of powder oxidation on the impact toughness of electron beam melting Ti-6Al-4V](#), *Additive Manufacturing* 17 (2017) 123–134. doi:[10.1016/j.addma.2017.08.002](https://doi.org/10.1016/j.addma.2017.08.002).  
URL <https://doi.org/10.1016/j.addma.2017.08.002>
- [13] C. Wei, X. Ma, X. Yang, M. Zhou, C. Wang, Y. Zheng, W. Zhang, Z. Li, [Microstructural and property evolution of Ti6Al4V powders with the number of usage in additive manufacturing by electron beam melting](#), *Materials Letters* 221 (2018) 111–114. doi:[10.1016/j.matlet.2018.03.124](https://doi.org/10.1016/j.matlet.2018.03.124).  
URL <https://doi.org/10.1016/j.matlet.2018.03.124>
- [14] R. Schur, S. Ghods, E. Schultz, C. Wisdom, R. Pahuja, A. Montelione, D. Arola, M. Ramulu, [A Fractographic Analysis of Additively Manufactured Ti6Al4V by Electron Beam Melting: Effects of Powder Reuse](#), *Journal of Failure Analysis and Prevention* (2020). doi:[10.1007/s11668-020-00875-0](https://doi.org/10.1007/s11668-020-00875-0).  
URL <https://doi.org/10.1007/s11668-020-00875-0>
- [15] C. Schade, G. K. N. Hoeganaes, Blending and Premixing of Metal Powders and Binders, *ASM Handbook 7 (Powder Metallurgy)* (2015) 88–92. doi:[10.31399/asm.hb.v07.a0006088](https://doi.org/10.31399/asm.hb.v07.a0006088).
- [16] H. P. Tang, M. Qian, N. Liu, X. Z. Zhang, G. Y. Yang, J. Wang, Effect of Powder Reuse Times on Additive Manufacturing of Ti-6Al-4V by Selective Electron Beam Melting, *Jom* 67 (3) (2015) 555–563. doi:[10.1007/s11837-015-1300-4](https://doi.org/10.1007/s11837-015-1300-4).
- [17] V. V. Popov, A. Katz-Demyanetz, A. Garkun, M. Bamberger, [The effect of powder recycling on the mechanical properties and microstructure of electron beam melted Ti-6Al-4V specimens](#), *Additive Manufacturing* 22 (June) (2018) 834–843. doi:[10.1016/j.addma.2018.06.003](https://doi.org/10.1016/j.addma.2018.06.003).  
URL <https://doi.org/10.1016/j.addma.2018.06.003>
- [18] D. Coney, M. Lasker, *Aerospace Structural Metals Handbook*, Code 3801, 1969.
- [19] N. Derimow, A. Romero, A. Rubio, C. Terrazas, N. Moser, O. L. Kafka, J. T. Benzing, F. Medina, R. Wicker, N. Hrabe, Assessment of intra-build variations in tensile strength in electron beam powder-bed fusion Ti-6Al-4V part 1: Effects of build height, Submitted for review (2022).
- [20] B. L. Boyce, B. C. Salzbrener, J. M. Rodelas, L. P. Swiler, J. D. Madison, B. H. Jared, Y. L. Shen, Extreme-Value Statistics Reveal Rare Failure-Critical Defects in Additive Manufacturing, *Advanced Engineering Materials* 19 (8) (2017) 1–10. doi:[10.1002/adem.201700102](https://doi.org/10.1002/adem.201700102).
- [21] B. C. Salzbrener, J. M. Rodelas, J. D. Madison, B. H. Jared, L. P. Swiler, Y. L. Shen, B. L. Boyce, [High-throughput stochastic tensile performance of additively manufactured stainless steel](#), *Journal of Materials Processing Technology* 241 (2017) 1–12. doi:[10.1016/j.jmatprotec.2016.10.023](https://doi.org/10.1016/j.jmatprotec.2016.10.023).  
URL <http://dx.doi.org/10.1016/j.jmatprotec.2016.10.023>
- [22] A. Du Plessis, I. Yadroitsev, I. Yadroitsava, S. G. Le Roux, X-Ray Microcomputed Tomography in Additive Manufacturing: A Review of the Current Technology and Applications, *3D Printing and Additive Manufacturing* 5 (3) (2018) 227–247. doi:[10.1089/3dp.2018.0060](https://doi.org/10.1089/3dp.2018.0060).

- [23] P. J. Withers, D. Grimaldi, C. K. Hagen, E. Maire, M. Manley, A. D. Plessis, [X-ray computed tomography](#), *Nature Reviews Methods Primers* 1 (18) (2021). doi:10.1038/s43586-021-00015-4.  
URL <http://dx.doi.org/10.1038/s43586-021-00015-4>
- [24] ASTM E2371-13, Standard Test Method for Analysis of Titanium and Titanium Alloys by Direct Current Plasma and Inductively Coupled Plasma Atomic Emission Spectrometry (Performance-Based Test Methodology) Coupled Plasma Atomic Emission Spectrometry ( ICP-AES ) 1, ASTM Standards (2013). doi:10.1520/E2371-13.2.
- [25] ASTM E1409-13, Standard Test Method for Determination of Oxygen and Nitrogen in Titanium and Titanium Alloys by Inert Gas Fusion, ASTM Standards (2013). doi:10.1520/E1409.
- [26] ASTM E1447-09, Standard Test Method for Determination of Hydrogen in Titanium and Titanium Alloys by Inert Gas Fusion Thermal Conductivity / Infrared Detection, ASTM Standards ((Reapproved 2016)) (2009). doi:10.1520/E1447-09R16.2.
- [27] ASTM E1941-10, Standard Test Method for Determination of Carbon in Refractory and Reactive Metals, ASTM Standards (2016). doi:10.1520/E1941-10.2.
- [28] Y. I. Ganor, A. Garkun, R. Z. Shneck, O. Yehekel, [Anelastic phenomena at room temperature in Ti6Al4V produced by electron beam powder bed fusion](#), *Additive Manufacturing* 54 (February) (2022) 102722. doi:10.1016/j.addma.2022.102722.  
URL <https://doi.org/10.1016/j.addma.2022.102722>
- [29] O. Tevet, D. Svetlizky, D. Harel, Z. Barkay, D. Geva, N. Eliaz, Measurement of the Anisotropic Dynamic Elastic Constants of Additive Manufactured and Wrought Ti6Al4V Alloys, *Materials* 15 (2) (2022). doi:10.3390/ma15020638.
- [30] G. Shanbhag, E. Wheat, S. Moylan, M. Vlasea, [Effect of specimen geometry and orientation on tensile properties of Ti-6Al-4V manufactured by electron beam powder bed fusion](#), *Additive Manufacturing* 48 (PA) (2021) 102366. doi:10.1016/j.addma.2021.102366.  
URL <https://doi.org/10.1016/j.addma.2021.102366>
- [31] A. I. Saville, S. C. Vogel, A. Creuziger, J. T. Benzing, A. L. Pilchak, P. Nandwana, J. Klemm-Toole, K. D. Clarke, S. L. Semiatin, A. J. Clarke, [Texture evolution as a function of scan strategy and build height in electron beam melted Ti-6Al-4V](#), *Additive Manufacturing* 46 (June) (2021) 102118. doi:10.1016/j.addma.2021.102118.  
URL <https://doi.org/10.1016/j.addma.2021.102118>
- [32] J. S. Tiley, Modeling of Microstructure Property Relationships in Ti-6Al-4V, The Ohio State University Doctoral T (2002) (2002) 192.
- [33] S. Kar, T. Searles, E. Lee, G. B. Viswanathan, J. Tiley, R. Banerjee, H. L. Fraser, Modeling the tensile properties in  $\beta$ -processed  $\alpha/\beta$  Ti alloys, *Metallurgical and Materials Transactions A: Physical Metallurgy and Materials Science* 37 (3) (2006) 559–566. doi:10.1007/s11661-006-0028-8.
- [34] I. Ghamarian, B. Hayes, P. Samimi, B. A. Welk, H. L. Fraser, P. C. Collins, [Developing a phenomenological equation to predict yield strength from composition and microstructure in  \$\beta\$  processed Ti-6Al-4V](#), *Materials Science and Engineering A* 660 (2016) 172–180. doi:10.1016/j.msea.2016.02.052.  
URL <http://dx.doi.org/10.1016/j.msea.2016.02.052>
- [35] N. Derimow, N. Hrabe, [Oxidation in Reused Powder Bed Fusion Additive Manufacturing Ti-6Al-4V Feedstock: A Brief Review](#), *Jom* 73 (11) (2021) 3618–3638. doi:10.1007/s11837-021-04872-y.  
URL <https://doi.org/10.1007/s11837-021-04872-y>